Comparison of propagation-based phase-contrast tomography approaches for the evaluation of dentin microstructure

Hans Deyhle[a], Timm Weitkamp[b,c], Sabrina Lang[a], Georg Schulz[a], Alexander Rack[c], Irene Zanette[b,d], and Bert Müller[a]

[a]Biomaterials Science Center, University of Basel, Basel, Switzerland;
[b]Synchrotron Soleil, Gif-sur-Yvette, France;
[c]European Synchrotron Radiation Facility, Grenoble, France;
[d]Department of Physics, Technische Universität München, Garching, Germany

ABSTRACT

The complex hierarchical structure of human tooth hard tissues, enamel and dentin, guarantees function for decades. On the micrometer level the dentin morphology is dominated by the tubules, micrometer-narrow channels extending from the dentin-enamel junction to the pulp chamber. Their structure has been extensively studied, mainly with two-dimensional approaches. Dentin tubules are formed during tooth growth and their orientation is linked to the morphology of the nanometer-sized components, which is of interest for example for the development of bio-inspired dental fillings. Therefore, a method has to be identified that can access the three-dimensional organization of the tubules, e.g. density and orientation. Tomographic setups with pixel sizes in the sub-micrometer range allow for the three-dimensional visualization of tooth dentin tubules both in phase and absorption contrast modes. We compare high-resolution tomographic scans reconstructed with propagation-based phase retrieval algorithms as well as reconstructions without phase retrieval concerning spatial and density resolution as well as rendering of the dentin microstructure to determine the approach best suited for dentin tubule imaging. Reasonable results were obtained with a single-distance phase retrieval algorithm and a propagation distance of about 75% of the critical distance of d^2/λ, where d is the size of the smallest objects identifiable in the specimen and λ is the X-ray wavelength.

Keywords: Synchrotron radiation-based micro computed tomography, phase contrast, signal-to-noise ratio, spatial resolution, dentin tubules, tooth microstructure, Paganin phase retrieval, segmentation

1. INTRODUCTION

The complex hierarchical structure of human tooth hard tissues, i.e. enamel and dentin, guarantees tooth function for decades. At the macroscopic level, the interplay of hard, brittle enamel and softer and tougher dentin allows for masticatory forces of up to 380 N [1]. On the micrometer level, the most prominent features are the dentin tubules, micrometer-narrow channels running from the pulp chamber to the dentin-enamel junction (DEJ) in an S-shaped fashion. Locally, they can appear wavy and tilted with respect to each other. They are surrounded by the highly mineralized peri-tubular dentin (PTD) and embedded in the intra-tubular dentin. Dentin tubuli are formed during tooth growth and mark the path of the odontoblasts, which ultimately determine the shape of the tooth. Since remodeling in dentin is minimal, their orientation is linked to the organization of the nanometer-sized components such as collagen fibers and calcium phosphate crystallites deposited during tooth formation [2,3]. These structures are of interest for example for the development of bio-inspired, anisotropic dental fillings with orientation dependent mechanical properties [4].

Dentin tubular structure [5–7] and its impact on the mechanical properties of dentin [8–10] have been studied with a wide variety of two-dimensional methods. These techniques often do not take into account local inhomogeneities related to tubule orientation. Therefore, a method has to be identified that gives access to the three-dimensional organization of the tubules. Tomographic setups with pixel sizes in the sub-micrometer range

Further author information: (Send correspondence to H.D.)
H.D.: E-mail: hans.deyhle@unibas.ch, Telephone: +41 61 265 9127

Developments in X-Ray Tomography VIII, edited by Stuart R. Stock,
Proc. of SPIE Vol. 8506, 85060N · © 2012 SPIE · CCC code: 0277-786/12/$18
doi: 10.1117/12.929951

allow for the three-dimensional (3D) visualization of tooth dentin tubules both in phase [11, 12] and absorption contrast modes [4, 13, 14]. Because of the small voxel size in these datasets, only small parts of a tooth, below approximately 1 mm in diameter, can be imaged simultaneously. Thus, for a complete understanding of the 3D organization of the tubular structure of dentin, scans of multiple thin specimens obtained from one tooth would be necessary from the present point of view. It is therefore desirable to identify the approach which allows one to image dentin tubules with the necessary spatial resolution as well as within reasonable scan time.

Absorption contrast is well suited for hard tissues such as bone or teeth, especially in a dry environment, due to the relatively high contrast of calcified tissues with respect to air, and thus suited for porous systems of these materials. Phase contrast techniques are particularly sensitive to interfaces, and therefore suitable for the detection of voids in an otherwise more or less homogeneous matrix, as is the case of dentin tubules, especially since exact information of dentin density is not needed.

Among X-ray phase contrast methods, grating interferometry (GI) excels due to its high density resolution [15], but it has only moderate spatial resolution [16]. It is therefore less suitable for imaging dentin tubuli. On the other hand, propagation-based (PB) phase contrast gives access to micrometer resolution [17]. In the present study we therefore investigated PB imaging approaches, which are based on phase contrast generated by the propagation of X rays in free space between specimen and detector. Phase retrieval was applied to the PB data with a multi-distance approach, frequently termed holotomography (HT) [18], and a single distance phase retrieval ($SDPR$) approach where the phase profile of the X-ray wavefront exiting plane of the specimen can be recovered from only a single radiograph, using an algorithm presented by Paganin *et al.* [19]. The algorithm assumes that monochromatic radiation illuminates a homogeneous object, a condition that is sufficiently fulfilled in the case of synchrotron radiation from a multilayer monochromator and dentin. In addition, the data acquired at different specimen-detector distances was reconstructed without phase retrieval.

The experimental data were compared concerning their spatial and density resolution, and rendering of the dentin microstructure, to determine the approach best suited for dentin tubule imaging and analysis. This knowledge is a prerequisite for the development of bio-inspired dental fillings or bio-inspired crown reconstructions.

2. MATERIALS AND METHODS

2.1 Specimen preparation

A 600×400 μm^2 thin rod was cut in the apical-cervical direction from the center of a human third molar, extracted for clinical reasons, with a diamond band saw (Exakt Apparatebau GmbH, Norderstedt, Germany). Enamel and a thin section of dentin below the DEJ were removed. The rod was dried in air prior to measurement.

2.2 Synchrotron radiation-based micro computed tomography

SRμCT measurements were performed at the beamline ID19 [20] at the European Synchrotron Radiation Facility (ESRF, Grenoble, France). The photon energy was set to 17.6 keV with a multilayer monochromator [20]. 1500 projections of 2048×2048 pixels each and a pixel size of 0.33 μm were acquired at equidistant angular positions over 180° while the specimen was continuously rotated. The exposure time for each projection was 1 s. Four scans were performed at distances z between specimen and detector of 3, 6, 9 and 20 mm.

2.3 Data treatment

2.3.1 Holotomography

Phase retrieval exploits the intensity modulations of the wavefront due to phase shifts caused by the specimen and subsequent propagation of the beam from specimen to detector. In the HT approach the phase shifts are determined from multiple projections acquired at different specimen-detector distances z [18]. For the phase retrieval from the four sets of data a mixed approach was chosen, which combines the contrast transfer function and the transport-of-intensity equation [21–23]. This algorithm is valid for non-zero specimen absorption and extended propagation distances. To reduce low-frequency artifacts, which can arise from the fact that the transfer function for phase contrast is small in the low spatial frequency range, the low-frequency components of the phase profile are assumed to be proportional to the logarithm of the projected intensity transmission via a

fixed estimate of the ratio δ/β of refractive index decrement over absorption coefficient [23]. A value of $\delta/\beta = 300$ was chosen, which yielded reasonable results even though it differs from the theoretical value of 130 at 17.6 keV [24].

2.3.2 Single distance phase retrieval

The phase profile of the X-ray wavefront exiting the plane of the specimen can be recovered from only a single radiograph under the assumption of a single material specimen and monochromatic illumination [19, 25]. Phase retrieval from single distance data was performed using the software *ANKAphase* [25] which is based upon an algorithm presented by Paganin *et al.* [19]. *ANKAphase* requires δ and β, the decrement of the real part of the refractive index and its imaginary part respectively, of the material to be known. The quality of the results is, however, only dependent on the ratio δ/β, while the absolute values of the two coefficients only result in a proportional scaling factor of the results. For processing, $\delta = 1.004 \cdot 10^{-6}$ and $\beta = 7.74 \cdot 10^{-9}$ were chosen, which are the δ and β values of hydroxy-apatite of 1.5 g·cm^{-3} density at 17.6 keV photon energy [24], resulting in a δ/β ratio of 130. Single distance phase retrieval was performed for the four acquired scans from the holotomography.

2.3.3 Tomographic reconstruction

All tomographic datasets were reconstructed using a filtered backprojection algorithm implemented in Matlab® (2010b, The MathWorks, Natick, USA).

3. RESULTS AND DISCUSSION

3.1 Density and spatial resolution

Figure 1 on the left shows a selected cross-section from the *HT* dataset of a tooth rod with a diameter of 500 μm. Despite the presence of prominent ring artifacts, the dentin can be described as rather homogeneous material, with the characteristic texture dominated by the dentin tubules. The white square indicates the region of interest (ROI) shown in the central panel of Figure 1. Here, the dentin tubules can be clearly identified as dark spots with a diameter between 1 and 2 μm, partially surrounded by structures with higher $\Delta\delta$. It is unclear whether these arise from electron density variations inside the dentin or are artifacts caused by specimen movement during the tomographic acquisition. The plot on the right shows the histogram of the 3D dataset. The peaks corresponding to air and dentin were individually fitted with Gaussians and are clearly separated. The shoulder on the left side of the dentin-related peak contains the dentin tubules, which exhibit intensities close to that of dentin due to the partial volume effect caused by the similar size of the tubules compared to the pixel size.

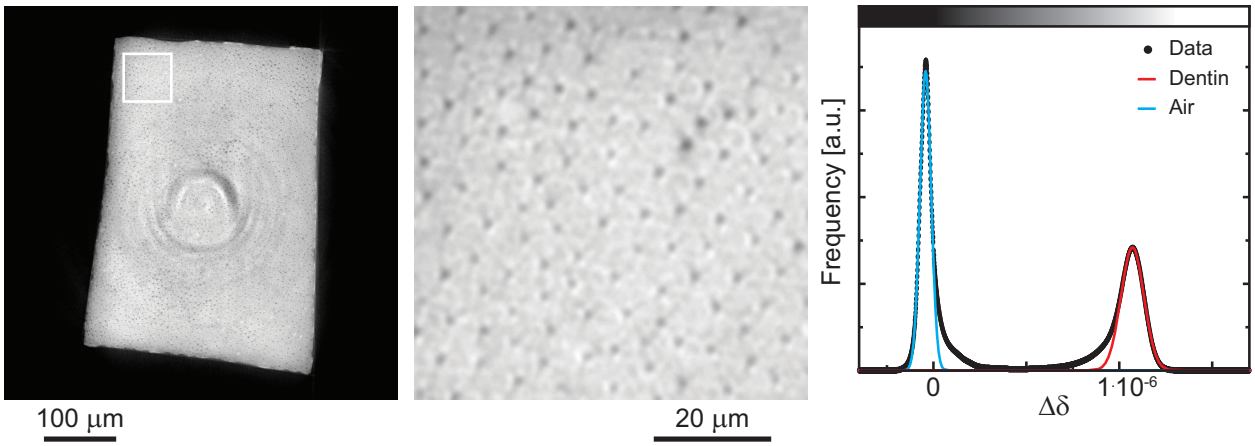

Figure 1. On the left, reconstructed slice of a 500 μm-thin tooth rod. The dentin appears speckled due to the presence of dentin tubules. In the center, magnified region according to the white square on the left. The dentin tubules can be clearly identified as dark spots. On the right, the histogram of the volumetric dataset. Air and dentin are clearly separated. The shoulder on the left of the dentin peak contains the dentin tubules, which exhibit intensities close to that of dentin due to the partial volume effect caused by the small size of the tubules, close to the pixel size of 0.33 μm.

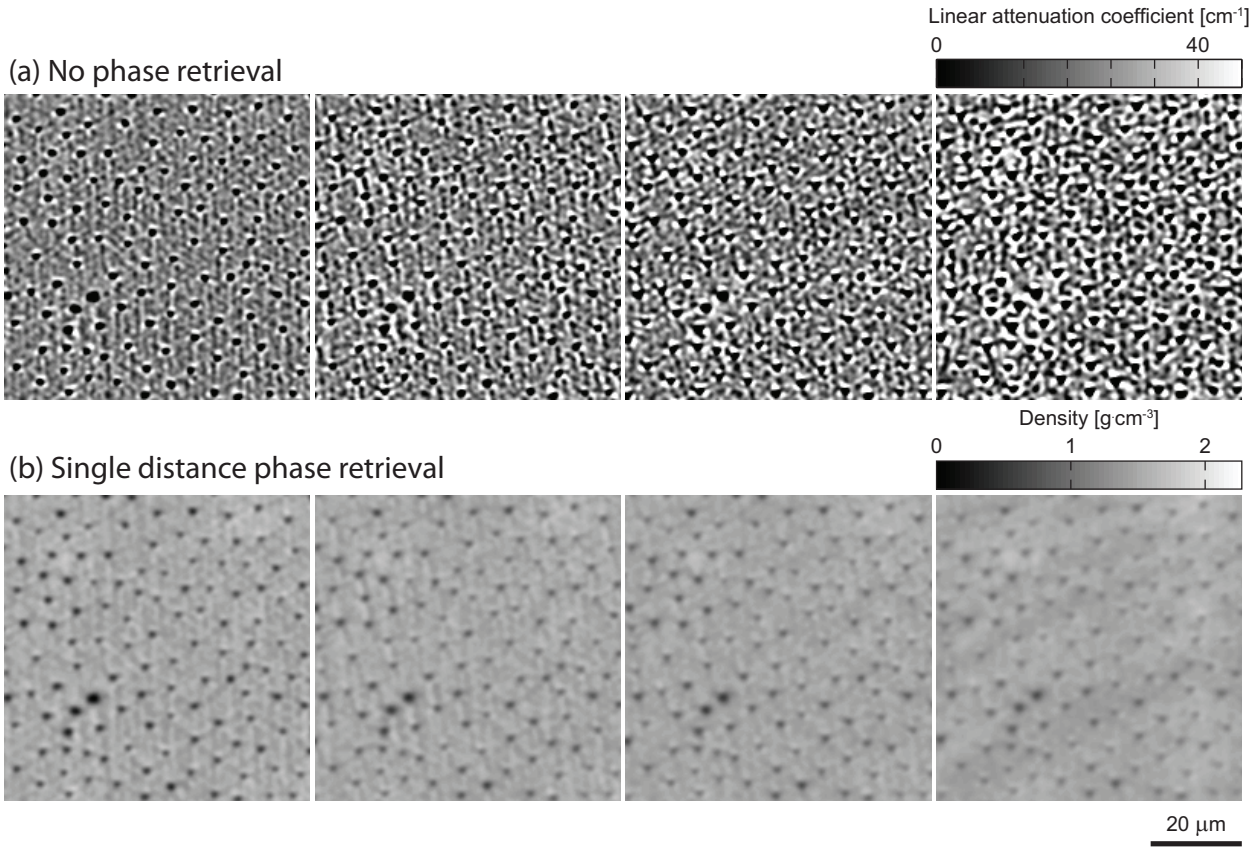

Figure 2. Detail of the specimen according to Figure 1. On the top line from left to right, a part of a selected slice from the data reconstructed without phase retrieval from the four measured distances (3, 6, 9 and 20 mm specimen-detector distance) are shown. Pronounced edge enhancement can be seen, it increases with specimen-detector distance. On the bottom line from left to right, the same region of the slice from the single distance phase retrieval data from the four measured distances. Note the increasing blurriness of the dentin tubules with longer specimen-detector distance.

Figure 2 shows, on the top row, a ROI of the data reconstructed without phase retrieval, acquired at the four specimen-detector distances 3, 6, 9 and 20 mm, from left to right respectively. The location of the ROI is defined in Figure 1. The dentin tubules can be identified as dark spots in the surrounding dentin matrix. While the dentin looks rather homogeneous in the data acquired at $z = 3$ mm, increasingly prominent bright structures surrounding the tubules, caused by edge enhancement, appear with increasing z, and inhomogeneities in the dentin increase. Zabler *et al.* showed that void tubules surrounded by a highly mineralized PTD give raise to dark spots surrounded by bright structures after free-space propagation of the X-rays if the radius of the PTD is at least 1.67 times as large as the radius of the void tubule [26]. The intensity of the bright rings is reported to increase with increasing propagation distance, in good agreement with our results. In the case of void tubules not surrounded by PDT they reported the presence of a bright spot at the position of the tubule after propagation. However, this case did not occur in the data presented here.

The bottom row shows the same ROI reconstructed from single distance phase retrieval projections. The tubules can be clearly identified in the leftmost image (3 mm specimen-detector distance) and become more and more blurry with increasing propagation distance.

Structures corresponding to the dentin tubules can be identified in the data of all imaging approaches even though their size and appearance vary depending on acquisition mode and z. It is therefore difficult to determine which approach offers the most accurate representation. A more thorough inspection of the spatial and density resolution of the datasets will allow for the choice of the most suited method.

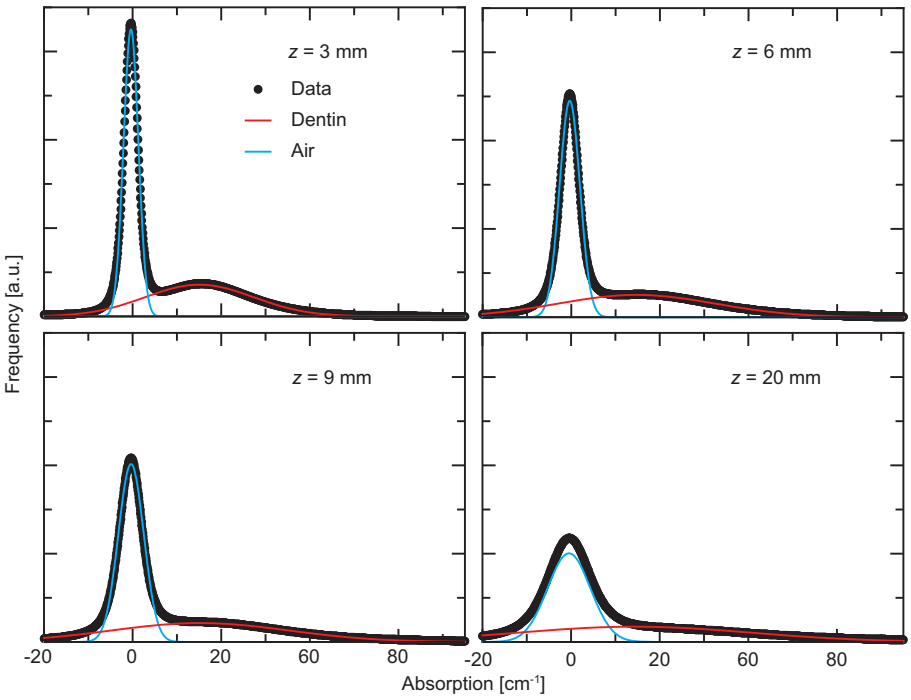

Figure 3. Histograms from the datasets reconstructed without phase retrieval, measured at the four specimen-detector distances 3, 6, 9 and 20 mm. The peak corresponding to dentin largely overlaps with the air-related peak and becomes broader with increasing specimen-detector distance while peak position remains largely unaffected.

Figures 3 and 4 show the attenuation coefficient and reconstructed density histograms ($SDPR$ data) of the 3D data, respectively, for the four specimen-detector distances. The peaks corresponding to air and dentin were fitted individually with Gaussians (pro Fit 6.2.0, Quantum Soft, Uetikon am See, Switzerland). The dentin-related peak from the data reconstructed without phase retrieval is almost an order of magnitude wider compared to the one related to the surrounding air. The width of both peaks increases with increasing z, indicating a degradation of density resolution. For the $SDPR$ data, however, the width of the dentin-related peak slightly decreases with increasing distance, from 0.22 full width at half maximum (FWHM) to 1.67 FWHM, as determined from the Gaussian fits (cp. Fig. 4), except for the last distance, where it increases to 0.23 FWHM. Therefore one expects an improvement in density resolution with increasing distance for this approach. The comparison of the histograms of the three approaches suggests that the large width of the dentin peak in the data reconstructed without phase retrieval does not originate solely from material inhomogeneities, but is rather a combination of X-ray absorption variations in the dentin and phase effects, e.g. edge enhancement.

To quantify the density resolution of the datasets, Herzen *et al.* [27] proposed the contrast-to-noise ratio (CNR) defined as

$$\mathrm{CNR} = \frac{|S_a - S_d|}{\sqrt{\sigma_a^2 + \sigma_d^2}} \tag{1}$$

where S_a and S_d are the peak positions (cp. Figs. 3 and 4) of the measured quantities corresponding to two different homogeneous materials, and σ_a and σ_d are the standard deviations in regions of equal volume inside these materials. Unfortunately, this approach is not directly applicable to the datasets discussed here since it requires two homogeneous media for the calculation of the standard deviations. Dentin can not be considered homogeneous for this purpose. Peri-tubular dentin and intra-tubular dentin are known to possess different degrees of calcification, and thus different densities. In addition, the high number of tubules present makes the selection of a volume containing only dentin difficult. Therefore the approach chosen by Schulz *et al.*

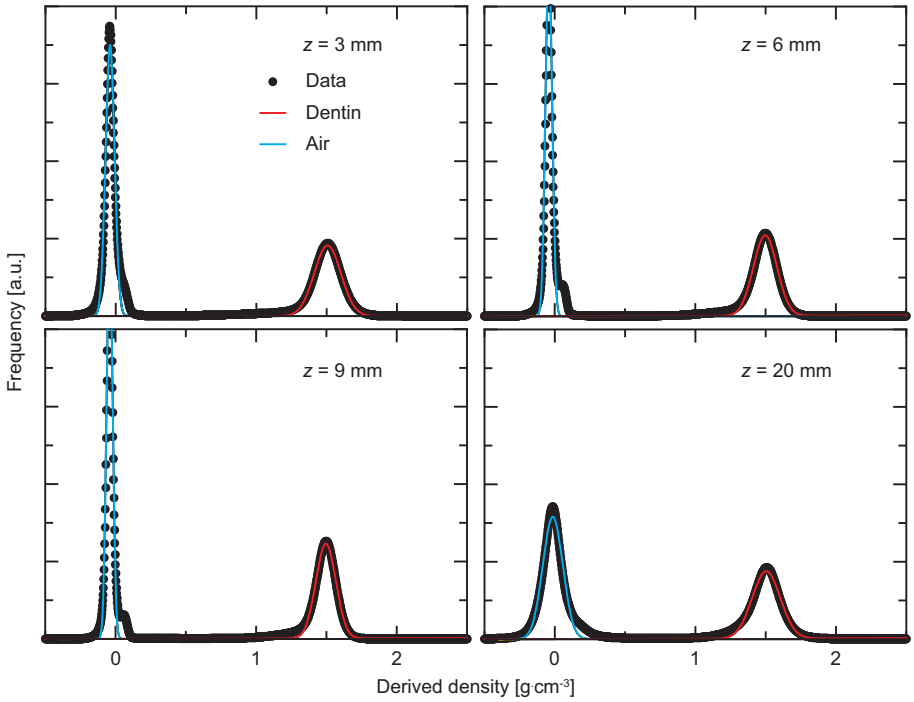

Figure 4. Single distance phase retrieval histograms from the datasets measured at the four specimen-detector distances 3, 6, 9 and 20 mm. The width of the dentin-related peak decreases from distance 1 through distance 3 while increasing again at distance 4.

[28] was applied, where only the standard deviation σ_a of the medium surrounding the specimen is considered. The single material contrast-to-noise ratio, CNR_{sm} is therefore defined as

$$\mathrm{CNR}_{sm} = \frac{|S_a - S_d|}{\sigma_a} \tag{2}$$

where S_d is the peak position of dentin, S_a the peak position of air and σ_a the standard deviation in a ROI in air. The CNR_{sm} are resumed in table 1. CNR_{sm} steadily decreases for the data reconstructed without phase retrieval with increasing specimen-detector distance. This is caused by the increased width of the air related peak, and therefore σ_a. We assume this is related to the appearance of streak-like noise which arises from the back projection of the enhanced edges in the specimen caused by longer propagation distances of the X rays between specimen and detector [29, 30]. On the contrary, CNR_{sm} increases up to 9 mm specimen-detector distance in the $SDPR$ data, while only the data at the maximal distance of 20 mm shows degraded density resolution. The algorithm proposed by Paganin *et al.* [19] is derived on the assumption that

$$z \ll \frac{d^2}{\lambda} \tag{3}$$

where z is the specimen-detector distance, d is the size of the smallest objects identifiable in the specimen and λ is the X-ray wavelength. For the present experiment $d \approx 1$ μm and $\lambda = 0.705$ Å. Therefore, the z should not exceed 10 mm. However, the phase retrieval algorithm proves to be robust against deviations from the optimal conditions [31]. Even though the CNR_{sm} decreases drastically at 20 mm, individual tubules can still be identified (cp. Fig. 2).

It is evident that the phase retrieval-based data outmatch the data without phase retrieval concerning density resolution. The highest CNR_{sm} is obtained for single distance phase retrieval data at $z = 9$ mm. It is almost a factor of 10 higher than one obtained from data reconstructed without phase retrieval acquired at $z = 3$ mm. Density resolution of the HT lies between the two methods discussed.

Table 1. Single material contrast-to-noise ratio CNR_{sm} for the investigated imaging approaches. z: specimen-detector distance, $SDPR$: single-distance phase retrieval.

Imaging approach	z **= 3 mm**	z **= 6 mm**	z **= 9 mm**	z **= 20 mm**
Without phase retrieval	9.2	6.6	5.4	3.1
SDPR	48.8	66.3	72.4	21.5
Holotomography		37.4		

To investigate the spatial resolution of the datasets, taking into consideration the properties of the specimen and experimental setup, the radial spectral power distribution (RSP) of a small region of the specimen of $201 \times 201 \times 201$ voxels was calculated and normalized by the RSP of a region of the same size containing air. The spatial resolution was defined as the highest spatial frequency where the normalized RSP had twice the baseline value [32, 33]. Table 2 lists the spatial resolution of the datasets.

The data reconstructed without phase retrieval yields the best spatial resolution among the investigated approaches in this study, ranging from 1.13 μm, which correspond to 3.4 pixels, at the shortest z to 1.36 μm, corresponding to 4.1 pixels, at $z = 20$ mm. Spatial resolution of the $SDPR$ data is found to be slightly degraded compared to the data reconstructed without phase retrieval. The difference between the two methods is however not as drastic as in the case of the CNR_{sm}. The origin of the improved spatial resolution in the $SDPR$ data for $z = 20$ mm is unclear. As should be expected, the spatial resolution in both approaches does not reach the theoretically optimal resolution limit imposed by the width of the first Fresnel zone of a point-like object in the specimen, given by $\sqrt{\lambda \cdot z}$, indicating that there are no spurious multiple fringes around object features, which would generate higher frequency contributions to the RSP. The resolution limit for the four specimen-detector distances z is also resumed in Table 2.

Table 2. Spatial resolution determined from the radial spectral power distribution for the investigated imaging approaches. Resolution is given in μm. z: specimen-detector distance, $SDPR$: single-distance phase retrieval.*Resolution limit* indicates the expected spatial resolution limit given by the width of the first Fresnel zone.

Imaging approach	**z = 3 mm**	**z = 6 mm**	**z = 9 mm**	**z = 20 mm**
Without phase retrieval	1.13	1.15	1.17	1.36
SDPR	1.67	1.88	2.13	1.86
Resolution limit	0.46	0.65	0.80	1.19
Holotomography		1.39		

The values for spatial resolution obtained by the RSP analysis (Table 2) are slightly better for the images obtained without phase retrieval than for the SDPR images. This is consistent with what should be expected because the SDPR phase reconstruction effectively acts as a low-pass filter on the spatial frequency spectrum of the data [19]. For the $SDPR$ data and the data obtained without phase reconstruction, the difference between the resolution values obtained by RSP analysis and the width of the first Fresnel zone decreases as the distance z increases. This is consistent with the expectations because at shorter distances z, the resolution should primarily be limited by experimental limitations as signal-to-noise ratio or detector resolution, whereas, at longer z, the Fresnel zone width should become the predominant resolution limit.

3.2 Tubule segmentation

Dentin tubules were segmented from the tomograms with a simple threshold approach and alternatively by filtering the individual slices with a second derivative kernel h:

$$h = \begin{pmatrix} 1 & 1 & 1 \\ 1 & -8 & 1 \\ 1 & 1 & 1 \end{pmatrix} \tag{4}$$

This filter was chosen since the the pixel size lies close to the characteristic size of the tubules which run perpendicular to the tomographic slices. After filtering, the slices were binarized to identify the pixels corresponding to tubules.

Since thresholding is related to image contrast, the first method was applied to the datasets of each imaging approach exhibiting the highest CNR_{sm}, while the second method, related to the presence of sharp edges, was applied to the datasets possessing highest spatial resolution. Figure 5 shows, on the top row, ROIs from the data reconstructed without phase retrieval, the $SDPR$ data and the HT data, from left to right. The pixels corresponding to the segmented tubules are shown in red. For the data reconstructed without phase retrieval, the segmentation threshold was chosen as the absorption value where the Gaussians related to air and dentin intersect. For the propagation-based methods, the threshold was defined as the value where the Gaussian fitted to the dentin-related peak reaches 10% of its maximum value. The bottom row of Figure 5 shows, analogously, the tomographic datasets and, superimposed in red, the tubules segmented with the filter approach.

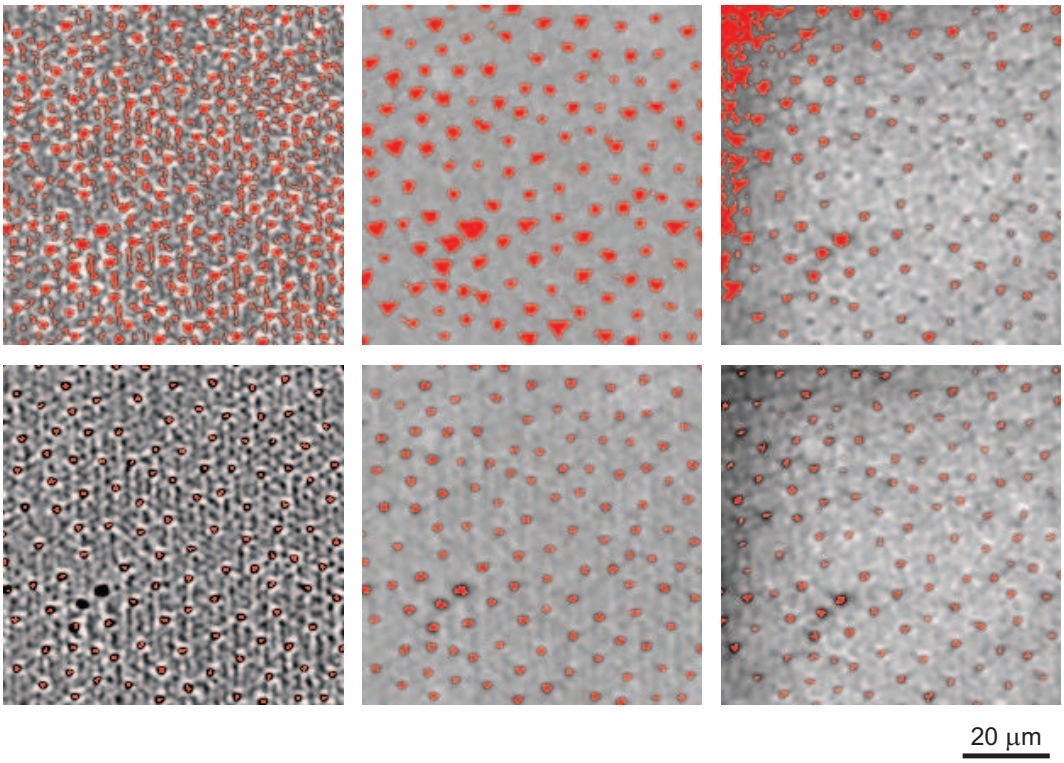

Figure 5. In the top row, from left to right, ROIs from the data reconstructed with no phase retrieval ($z = 3$ mm), with $SDPR$ ($z = 9$ mm) and HT. Segmented dentin tubules (in red) were superimposed to the tomograms. In the top row, a thresholding approach was chosen for segmentation. In the bottom row, ROIs from the data reconstructed with no phase retrieval ($z = 3$ mm), with $SDPR$ ($z = 3$ mm) and HT are shown, analogously. Segmentation was performed with a second derivative filtering and subsequent thresholding.

Segmentability through thresholding is in reasonable agreement with the CNR_{sm} values, i.e. better contrast leads to better segmentability. Thresholding of the data reconstructed without phase retrieval leads to the inclusion of structures within the dentin due to the high inhomogeneity in the material, in agreement with the fact that the air- and dentin-related curves in Fig. 3 overlap. $SDPR$ data after thresholding show satisfying

results concerning tubule position, however the mean tubule diameter is above those determined with the other approaches. We assume that through this segmentation procedure their size is overestimated. The spatial resolution of the shown dataset amounts to 1.7 μm, which is near the mean diameter of the tubules. The tubule edges do therefore not appear sharp and are smeared over the complete area of the tubules and surrounding dentin. Thus, the tubules exhibit a contrast value closer to dentin rather than air. The threshold was chosen to be high enough that the majority of tubules were segmented. The consequence is that an increased number of voxels is considered part of the tubules. A more conservative threshold would lead to a more precise estimation of tubule sizes, but on the other hand also be less sensitive to the smaller voids. Such an approach can be seen in the threshold-segmented HT-data (top-right in Fig. 5), where size and position of the larger tubules is segmented correctly, while smaller tubules remain undetected.

Segmentation based on the second derivative of the data yields overall better results than the threshold-based approach (bottom row of Fig. 5). The sharp edges in the tomogram of the data reconstructed without phase retrieval, related to the high spatial resolution, lead to an underestimation of the tubule size with the applied filter, and large tubules are not detected at all. A larger filter kernel could lead to an improvement of the segmentation. The blurriness of the $SDPR$ data is, in this case, of advantage, since the tubule edges do not appear sharp. Therefore, larger structures are also segmented. This is also the case for the HT data, where position and size of all tubules can be extracted.

4. CONCLUSIONS

High-resolution SRμCT is a suitable tool for the 3D imaging of human teeth, allowing for the rendering of the dentin tubules, which dominate the tooth microstructure. The propagation-based phase retrieval approaches offer increased density resolution compared to the data where no phase retrieval was performed, while still retaining sufficient spatial resolution for tubule identification. This has the advantage of a better representation of modulations in dentin density. Therefore, these approaches will often be preferred over reconstructions with no phase retrieval, since the complexity of the setup and data processing only slightly exceed those of measurements without phase retrieval. Since single distance phase retrieval and holotomography achieve comparable results, the manifold acquisition time in holotomography, caused by the necessity for multiple scans at different detector distances, makes $SDPR$ the better alternative. The best results in this study are achieved with a propagation distance of about 75% of the critical distance of d^2/λ.

REFERENCES

[1] Helkimo, E., Carlson, G. E., and Helkimo, M., "Bite force and state of dentition," *Acta Odontol. Scand.* **35**, 207–303 (1977).

[2] Deyhle, H., Bunk, O., and Müller, B., "Nanostructure of healthy and caries-affected human teeth," *Nanomed-Nanotechnol.* **7**, 694–701 (2011).

[3] Gaiser, S., Deyhle, H., Bunk, O., White, S. N., and Müller, B., "Understanding nano-anatomy of healthy and carious human teeth: A prerequisite for nanodentistry," *Biointerphases* **7**, 4 (2012).

[4] Deyhle, H., Bunk, O., Buser, S., Krastl, G., Zitzmann, N. U., Ilgenstein, B., Beckmann, F., Pfeiffer, F., Weiger, R., and Müller, B., "Bio-inspired dental fillings," *Proc. SPIE* **7401**, 74010E (2009).

[5] Schilke, R., Lisson, J. A., Bauss, O., and Geurtsen, W., "Comparison of the number and diameter of dentinal tubules in human and bovine dentine by scanning electron microscopic investigation," *Arch. Oral Biol.* **45**, 355–361 (2000).

[6] Schellenberg, U., Krey, G., Bosshardt, D., and Nair, P. N. R., "Numerical density of dentinal tubules at the pulpal wall of human permanent premolars and third molars," *J. Endod.* **18**, 104–109 (1992).

[7] Mjör, I. A. and Nordahl, I., "The density and branching of dentinal tubules in human teeth," *Arch. Oral Biol.* **5**, 401–412 (1996).

[8] Nalla, R. K., Kinney, J. H., and Ritchie, R. O., "Effect of orientation on the in vitro fracture toughness of dentin: The role of toughening mechanisms," *Biomater.* **24**, 3955–3968 (2003).

[9] Inoue, S., Pereira, P. N. R., Kawamoto, C., Nakajima, M., Koshiro, K., Tagami, J., Carvalho, R. M., Pashley, D. H., and Sano, H., "Effect of depth and tubule direction on ultimate tensile strength of human coronal dentin," *Dent. Mater. J.* **22**, 39–47 (2003).

[10] Kinney, J. H., Marshall, S. J., and Marshall, G. W., "The mechanical properties of human dentin: A critical review and re-evaluation of the dental literature," *Crit. Rev. Oral Biol. Med.* **14**, 13–29 (2003).

[11] Zabler, S., Cloetens, P., and Zaslansky, P., "Fresnel-propagated submicrometer X-ray imaging of water-immersed tooth dentin," *Opt. Lett.* **32**, 2987–2989 (2007).

[12] Zaslansky, P., Zabler, S., and Fratzl, P., "3D variations in human crown dentin tubule orientation: A phase-contrast microtomography study," *Dent. Mater.* **26**, e1–e10 (2010).

[13] Stock, S. R., Vieira, A. E. M., Delbem, A. C. B., Cannon, M. L., Xiao, X., and De Carlo, F., "Synchrotron microcomputed tomography of the mature bovine dentinoenamel junction," *J. Struct. Biol.* **161**, 162–171 (2008).

[14] Parkinson, C. R. and Sasov, A., "High-resolution non-destructive 3D interrogation of dentin using X-ray nanotomography," *Dent. Mater.* **24**, 773–777 (2008).

[15] Zanette, I., Weitkamp, T., Lang, S., Langer, M., Mohr, J., David, C., and Baruchel, J., "Quantitative phase and absorption tomography with an X-ray grating interferometer and synchrotron radiation," *Phys. Status Solidi A* **208**, 2526–2532 (2011).

[16] Lang, S., Zanette, I., Dominietto, M., Langer, M., Rack, A., Le Duc, G., David, C., Mohr, J., Pfeiffer, F., Müller, B., and Weitkamp, T., "Comparison of grating-based and propagation-based X-ray phase tomography of soft tissue," **in preparation** (2012).

[17] Spanne, P., Raven, C., Snigireva, I., and Snigirev, A., "In-line holography and phase-contrast microtomography with high energy X-rays," *Phys. Med. Biol.* **44**, 741–749 (1999).

[18] Cloetens, P., Ludwig, W., Baruchel, J., Van Dyck, D., Van Landuyt, J., Guigay, J. P., and Schlenker, M., "Holotomography: Quantitative phase tomography with micrometer resolution using hard synchrotron radiation X rays," *Appl. Phys. Lett.* **75**, 2912–2914 (1999).

[19] Paganin, D., Mayo, S. C., Gureyev, T. E., Miller, P. R., and Wilkins, S. W., "Simultaneous phase and amplitude extraction from a single defocused image of a homogeneous object," *J. Microsc.* **206**, 33–40 (2002).

[20] Weitkamp, T., Tafforeau, P., Boller, E., Cloetens, P., Valade, J.-P., Bernard, P., Peyrin, F., Ludwig, W., Helfenand, L., and Baruchel, J., "Status and evolution of the ESRF beamline ID19," *AIP Conf. Proc.* **1221**, 33–38 (2010).

[21] Guigay, J., Langer, M., Boistel, R., and Cloetens, P., "Mixed transfer function and transport of intensity approach for phase retrieval in the Fresnel region," *Opt. Lett.* **32**, 1617–1619 (2007).

[22] Langer, M., Cloetens, P., Guigay, J. P., and Peyrin, F., "Quantitative comparison of direct phase retrieval algorithms in in-line phase tomography," *Med. Phys.* **35**, 4556–4566 (2008).

[23] Langer, M., Cloetens, P., and Peyrin, F., "Regularization of phase retrieval with phase-attenuation duality prior for 3D holotomography," *IEEE Trans. Image Proces.* **19**, 24282436 (2010).

[24] "CXRO center for x-ray optics," *http://henke.lbl.gov/optical_constants/getdb2.html* .

[25] Weitkamp, T., Haas, D., Wegrzynek, D., and Rack, A., "ANKAphase: software for single-distance phase retrieval from inline X-ray phase-contrast radiographs," *J. Synchrotron Rad.* **18**, 617–629 (2011).

[26] Zabler, S., Riesemeier, H., Fratzl, P., and Zaslansy, P., "Fresnel-propagated imaging for the study of human tooth dentin by partially coherent x-ray tomography," *Opt. Express* **14**, 8584–8597 (2006).

[27] Herzen, J., Donath, T., Pfeiffer, F., Bunk, O., Padeste, C., Beckmann, F., Schreyer, A., and David, C., "Quantitative phase-contrast tomography of a liquid phantom using a conventional X-ray tube source," *Opt. Express* **17**, 1001010018 (2009).

[28] Schulz, G., Waschkies, C., Pfeiffer, F., Zanette, I., Weitkamp, T., David, C., and Müller, B., "Multimodal imaging of human cerebellum - merging X-ray phase microtomography, magnetic resonance microscopy and histology," **submitted** (2012).

[29] Cloetens, P., Barrett, R., Baruchel, J., Guigay, J. P., and Schlenkerz, M., "Phase objects in synchrotron radiation hard X-ray imaging," *J. Phys. D* **29**, 133–146 (1996).

[30] Snigirev, A., Snigireva, I., Kohn, V., Kuznetsov, S., and Schelokov, I., "On the possibilities of xray phase contrast microimaging by coherent high energy synchrotron radiation," *Rev. Sci. Instrum.* **66**, 5486–5492 (1995).

[31] Myers, G. R., Mayo, S. C., Gureyev, T. E., Paganin, D. M., and Wilkins, S. W., "Polychromatic cone-beam phase-contrast tomography," *Phys. Rev. A* **76**, 045804 (2007).

[32] Modregger, P., D., Lübbert, Schäfer, P., and Köhler, R., "Spatial resolution in Bragg-magnified X-ray images as determined by Fourier analysis," *Phys. Status Solidi A* **204**, 2746–2752 (2007).

[33] Schulz, G., Weitkamp, T., Zanette, I., Pfeiffer, F., Beckmann, F., David, C., Rutishauser, S., Reznikova, E., and Müller, B., "High-resolution tomographic imaging of a human cerebellum: Comparison of absorption and grating based phase contrast," *J. R. Soc. Interface* **7**, 1665–1676 (2010).